Remote Sensing of Environment 264 (2021) 112580

Contents lists available at ScienceDirect

Remote Sensing of Environment

journal homepage: www.elsevier.com/locate/rse

Precise inland surface altimetry (PISA) with nadir specular echoes from Sentinel-3: Algorithm and performance assessment

R. Abileah [a], S. Vignudelli [b,*]

[a] jOmegak, San Carlos, CA, USA
[b] Consiglio Nazionale delle Ricerche (CNR-IBF), Italy

ARTICLE INFO

Edited by Menghua Wang

Keywords:
Satellite radar altimetry
Altimeter bursts
Water level
Specular inland water bodies
Radar cross section
Sentinel-3
Salar de Uyuni

ABSTRACT

In the recent years satellite radar altimetry has evolved from pulse-limited low resolution mode (LRM) to a synthetic aperture radar (SAR) high resolution mode. The SAR mode focusses and coherently sums all radar return echoes within the 2-s time window the target surface area is in the antenna beam. In principle the SAR processing improves along-track resolution. Land contamination has been a major concern for inland waters altimetry and SAR can reduce land interference. This paper shows that the physics of specular echoes from smooth inland waters leads to a very different approach which we call precise inland surface altimetry (PISA). PISA uses only echoes within the specular "flash" period, which is approximately the time the satellite nadir crosses over the water body. The processing is four orders of magnitude less than SAR. Land interference is negligible because specular water echoes are usually >50 dB greater than land. Sentinel-3 SRAL dataset on the salar de Uyuni (Bolivia) is used to evaluate PISA ranging precision. During inundation (wet months), echoes are at the theoretical maximum radar cross section (RCS), σ = 129 dBsm, and ranging precision is ~1 mm. In dry months the echoes are quasi-specular, with σ = 70–100 dBsm, and ranging precision is ~1 cm. The precision assessment is made with variate-differences, with pass-to-pass repeatability, and by comparison with GPS measurements. In addition to the salar de Uyuni analysis we gathered σ statistics on five millions Sentinel-3 SRAL Ku-band altimeter bursts (one burst = 64 contiguous echoes) from 52 passes of Sentinel-3A track 167 over South America. We illustrate specular and quasi-specular waters on lakes, a river, and a fjord. Ranging precision is similar to Uyuni, in the 1 mm-1 cm range. Water surface slopes of 1–3 cm/km are detected. We propose a simple rule-set to distinguish specular waveforms (σ >100 dBsm, sidelobes (with Hamming window) of −37 dB or lower) and quasi-specular (σ >70 dBsm, sidelobes lower than −20 dB), and non-specular (sidelobes> − 20 dB). PISA is appropriate to specular and quasi-specular echoes.

1. Introduction

Satellite radar altimetry is rapidly undergoing a paradigm shift from non-Doppler to Doppler-based processing methods. The Doppler-based (also referred to as synthetic aperture radar (SAR)) processing methods include the delay-Doppler algorithm (Raney, 1988), the SAR Versatile Altimetric Toolkit for Ocean Research & Exploitation (SARvatore) (Dinardo, 2020), and the fully focused SAR (FF-SAR) altimetry (Egido and Smith, 2016). This paper introduces a fourth Doppler-based method: the precision inland surface altimetry (PISA), which is specifically formulated for specular echoes from calm surfaces.

1.1. Early work

Doppler processing algorithms require downlinking the in-phase (I) and quadrature (Q) components of the radar signal of each pulse for ground-based processing. The IQ data is an order of 10^3 increase in the downlink bandwidth relative to the 20 Hz (non-Doppler) low-resolution mode (LRM) processing of the previous era. When Doppler processing was first proposed three decades ago by Raney (1988), such downlink bandwidths were technically infeasible. In 2002, the European Space Agency launched the Envisat satellite to continue producing the LRM products of earlier altimeters. However, a limited amount of IQ data in 1-s bursts at one-minute intervals was downlinked to encourage early experimentation with Doppler/SAR processing (Berry et al., 2007).

* Corresponding author at: Consiglio Nazionale delle Ricerche (CNR-IBF) c/o Area della Ricerca CNR, Via Moruzzi 1, 56127 Pisa, Italy.
E-mail addresses: abileah@jOmegak.com (R. Abileah), stefano.vignudelli@ibf.cnr.it (S. Vignudelli).

https://doi.org/10.1016/j.rse.2021.112580
Received 4 November 2020; Received in revised form 21 June 2021; Accepted 29 June 2021
Available online 29 July 2021

Abileah et al. (2013) applied the IQ in a 'zero-Doppler averaging' which means coherent summing of echoes assuming range is constant. This was an early version of the PISA algorithm. Quartly and Passaro (2015) studied the zero-Doppler method with AltiKa satellite.

Abileah et al. (2017) applied the zero-Doppler method on inland waters and demonstrated sub-cm range precision with specular echoes. For example, on Rio Nahuapa (Peru), root mean-squared error (rmse) was 4 mm. Such precision was an order of magnitude better than LRM range estimates (ESA, 2017).

The concept of coherently integrating more echoes was furtherly developed with FF-SAR. On a transponder overpass located on Svalbard Islands the rmse in echo phase was demonstrated to be 3%, equivalent to 0.2 mm in round trip distance (Egido and Smith, 2016). This result is a testimonial of the remarkable phase stability of the radar and accuracy of the orbital determination. It was suggested that a real-world application is ranging inland water bodies. FF-SAR would 'focus' on a water surface and 'un-focus' land clutter, thereby improving range estimation for lakes and rivers to an unprecedented precision. Kleinherenbrink et al. (2020) applied FF-SAR to lakes, rivers, canals, and ditches in the Netherlands.

1.2. PISA relation to FF-SAR

Altimeters installed on onboard satellites use frequency-modulated continuous-wave (FMCW) radars. As in all FMCW radars, the return echoes are mixed with delayed replicas of the transmitted pulses, and the mixed signals are downsampled and downlinked to ground-based processing. For Doppler processing methods the ground processing involves coherent integration of some/many echoes, followed with pulse compression, then inversion of the range waveform into a range estimate. The various Doppler processing methods differ mostly in the details of the coherent integration.

What follows explains specifically how PISA differs from the FF-SAR (Egido and Smith, 2016) as adapted to inland waters by Kleinherenbrink et al. (2020). Some details (e.g., satellite vertical velocity) will be ignored for brevity and to emphasize key differences in respect to processing specular echoes. For illustration, it is assumed that an altimeter radar track is crossing over and perpendicular to a 100 m wide river.

Both Doppler processing methods start with prior knowledge of the water body boundary, given in a form of a 0–1 geographical water mask. A number of world water mask data bases exist (e.g., Pekel et al., 2016). Google Earth is another good resource for this purpose.

FF-SAR uses all ten thousand echoes within a 1.9 s SAR window. PISA uses only the ~100 echoes when the nadir is directly over the water body. The underlying logic is that with specular echoes there is very little signal outside the specular flash.

FF-SAR picks a ground point within the water mask. A range migration is applied to all ten thousand echoes to account for the satellite position with respect to the ground point. Here is the second important difference: PISA has no range migration correction since all the echoes are when nadir is over an (assumed) flat water surface and, therefore, there is no range migration (more about this in Section 2.3).

Next the echoes are coherently summed. The summed waveform is fft'ed. into the range-waveform. This step is the same in both algorithms. But there is an important third difference at this point. The FF-SAR waveform is 'focused' on one point on the Earth surface. PISA is 'focused' on the entire river width and is now done with echo processing. FF-SAR is repeated at all points within the water mask, spaced 0.5 m along track for a total of 200 focus points called 'looks' in Kleinherenbrink et al. (2020). The computational complexity is an order of 10^4 greater than PISA.

There is one further difference between the algorithms in inverting the waveform into range, or what is commonly referred to as 'retracking' in the altimetry literature. Kleinherenbrink et al. (2020) use the SAMOSA+ retracker which allows multiple peaks (possibly interference) and non-specular surface backscatter (wind roughened surface). In PISA the range estimate is simply the peak in the range waveform.

1.3. Occurrences of specularity

PISA is specifically developed for specular echoes. The Rayleigh criterion for specular reflection is a surface height variation $< \lambda/(8\cos(\Theta))$, with λ being the carrier wavelength (Table 1) and Θ is the angle of incidence (Murphy, 2006). In the case of nadir incidence, $\Theta = 0°$, therefore, the Rayleigh criterion for specularity is a surface roughness scale of $< \lambda/8$ or < 3 mm for the Sentinel-3 Ku band radar. PISA is useful only if such degree of smoothness occurs frequently.

Table 1
Notations and parameter values used in the PISA algorithm specific to Sentinel 3 constellation and level 1A data provided by ESA.

Parameter	Notation	Value	Name-value in ESA provided netcdf (nc) files
Speed of light	c	299,792,458 m/s	
Carrier frequency	f_c	13.57532 GHz	
Carrier wavelength	λ	$c/f_c = 0.0220870$ m	
Carrier wavenumber	κ	$2\,\pi/\lambda$	
Bandwidth	B	320 MHz	
Pulse duration	T_p	44.8 μs	
IF sample time	dt	$T_p/128 = 3.5\ 10^{-7}$ s	
Fast time	t	$-T_p/2, -T_p/2 + dt, \ldots, T_p/2$	
Chirp frequency rate	α	$B/T_p = 7.1429\ 10^{12}$ Hz/s	
Pulse repetition frequency	PRF	17.825 kHz	
Number of pulses in a burst	N_b	64	
Range, radar to scattering surface	R		
Range to surface at the nadir	R_0		
Two-way time delay	τ	$\frac{2R}{c}$	
Tracker range (reference range)	R_{tkr}		range_ku_l1a_echo_sar_ku
Two-way time delay relative to R_{tkr}	τ_{tkr}	$\frac{2(R - R_{tkr})}{c}$	
Orbital height	H	815 km (average)	alt_l1a_echo_sar_ku
Satellite vertical velocity	v_r	−15 to +25 m/s depending on location	orb_alt_rate_l1a_echo_sar_ku
GPS Correction	Δ_{gps}	$=0.2976 \times (0.3333333333\text{-sin(latitude)}^2) \times 0.6078$	
Geo correction	Δ_{geo}		Provided externally. It includes atmospheric and crustal corrections
CoG correction	Δ_{cog}	0.5559 m	cog_cor_l1a_echo_sar_ku
Gain control adjustment	AGC		agc_ku_l1a_echo_sar_ku
Radar cross section	σ	0 to 129 dBsm (explained in the text)	
σ scaling factor	*SigmaScaling*		scale_factor_ku_l1a_echo_sar_ku
Nadir track latitude and longitude			lat_l1a_echo_sar_ku lon_l1a_echo_sar_ku

As yet there is no quantitative analysis of the frequency of specular water echoes. A variety of inland water bodies have been found to be specular (Abileah et al., 2017, 2018), including: rivers in the Peruvian Amazon; the Tonle Sap flood plain; a 4-km wide Lacohloosa Lake, Florida; Lake Tuz (a salt lake) in Turkey; Tennessee River; and others. Some water bodies such as the Arno River (Italy) and nearby canale Usciana, are specular most or all times (based on three years of revisits). In the very large river category a considerable variability was observed: the braided Congo River is specular; the 350 m wide Rio Tigre, specular only 50% of the time; the 500 m wide Ohio River, specular 12% of the time at one location, 0% at another; on the Mississippi River only occasional quasi-specular echoes are observed. More examples of real-world specular water are in this paper, including the first discovery of a specular fjord, two large lakes in the Andes, and many specular flashes in the Brazilian Amazon and the Delta Amacuro (Venezuela) region.

1.4. Precision vs accuracy

The goal of satellite radar altimetry is creating a worldwide network of virtual water gauges. The satellite radar altimetry processing problem can be divided into three parts: 1) the coherent zero-Doppler sum of a burst of individual echoes; 2) estimating the radar range and 3) translating range into surface levels. We refer to error in ranging as *precision* and error in surface levels as *accuracy*. Accuracy involves both ranging precision and additional factors such as errors in modeling wet and dry topo factors (Fu and Cazenave, 2000), which are the same for all the Doppler altimeters.

The remainder of this paper is organized in three main sections. Section 2 covers the theory of specular targets necessary to discuss the algorithm. Section 3 describes the PISA algorithm. Section 4 presents evaluations of the PISA ranging *precision* on real-world data. Surface level accuracy is not in the scope of this paper. Table 1 lists the notations for the physical and system parameters used in the text, with values specific to the Sentinel-3 SRAL Ku-band altimeter.

2. Numerical model of a specular echo

The echo from a specular surface is a sum of all the elemental scatterers, each with area *dS*

$$z(n) = \frac{2\sqrt{\pi}dS}{\lambda} \sum_{i\epsilon M} e^{-i\varphi_i\,(n)} \tag{1}$$

(Skolnik, 1990; Collins et al., 1998). Backscatter from land surrounding the water body is assumed negligible. The sum includes only water scatters; M is the water mask. The factor $2\sqrt{\pi}dS/\lambda$ scales the model into units of $\sqrt{\sigma}$, where σ is the radar cross section (RCS), *n* is the time instant, and $\varphi_i\,(n)$ is the corresponding phase of the *i*-th scatterer, which depends on the range from the satellite to the elemental scatterer at that instant. Using Eq. (1), it is possible to precisely predict complex radar echoes for arbitrary water surface sizes and shapes, with the radar positioned either directly over the water body or squinting on an off-nadir water surface. Patches of surface roughness can be included as random additions to the phases. In this paper, only simple shapes (disk and rectangular) and perfectly flat water surfaces are considered. The numerical accuracy of Eq. 1 improves with the dS tending to 0. With $dS = 0.2\ m^2$, the numerical RCS converged on the theoretical near-field RCS (Pouliguen et al., 2008). For this reason, the value $dS = 0.2\ m^2$ is used for all of the following model calculations.

2.1. Specular flash

Eq. 1 was used to calculate the duration of specular flash for disk-shaped 'lakes' of varying diameters (Fig. 1) and rectangle-shaped 'river' with varying widths (Fig. 3). The river length is perpendicular to the altimeter track. The colour bar is σ from Eq. 1. The along-track axes refer to the nadir locations. The satellite nadir approaches the water body from the left; the zero value is the centerline and closest point of approach (CPA) to the water surface center (for a lake) or centerline (for a river). These numerical results are compared with Pouliguen's model at along-track 0 (Figs. 2 and 4).

With reference to lakes (Fig. 1), the flash duration is U-shaped with respect to the width, with a minimum at ~100 m. The 100-m minimum was also noted in our earlier paper (Abileah et al., 2017). For lakes of diameters >100 m, the flash period is approximately equal to the time required for the altimeter nadir track to cross over the water body. Since the satellite nadir velocity is 7 km/s, the flash duration is typically <0.1 s. The echo power diminishes perceptibly when the nadir is outside the water-surface boundaries, reduced 25 dB at a distance of 200 m from the water edge and 35 dB at a distance of 1 km from the boundary. The implication here is that a water mask has to be used to identify the echoes when the satellite nadir is located over the water body of interest. Only those echoes should be used, which is the novel idea in PISA.

2.2. Radar cross section (σ) at CPA

The theoretical near-field σ given by Pouliguen et al. (2008) (Eq. 9) is

$$\sigma = 2\pi R^2 \left\{ a - cos\left(\frac{ka^2}{R}\right) \right\} \tag{2}$$

where k is the carrier wavenumber (Table 1). It applies to a disk at nadir,

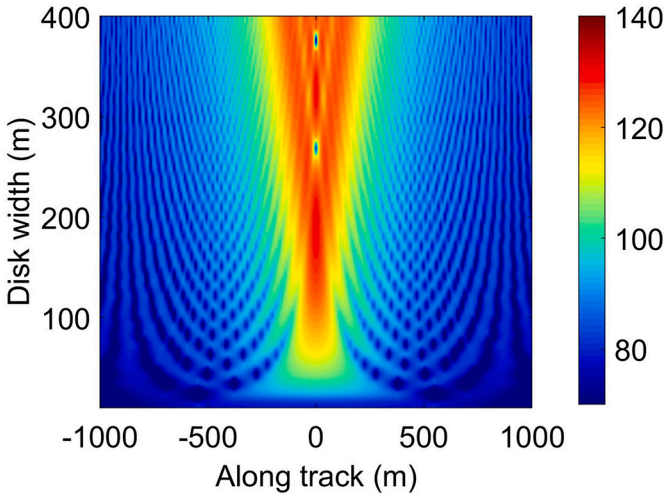

Fig. 1. Along-track specular σ (dBsm) for disk-shaped 'lakes' of varying diameters.

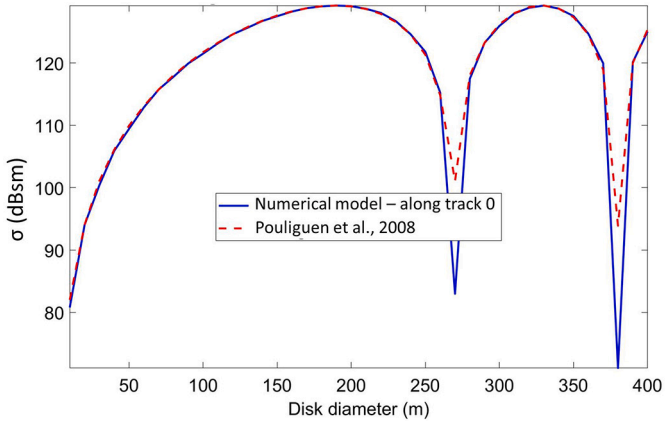

Fig. 2. σ (dBsm) of the numerical model for nadir centered on lakes and the model by Pouliguen et al. (2008) for disks of varying diameters.

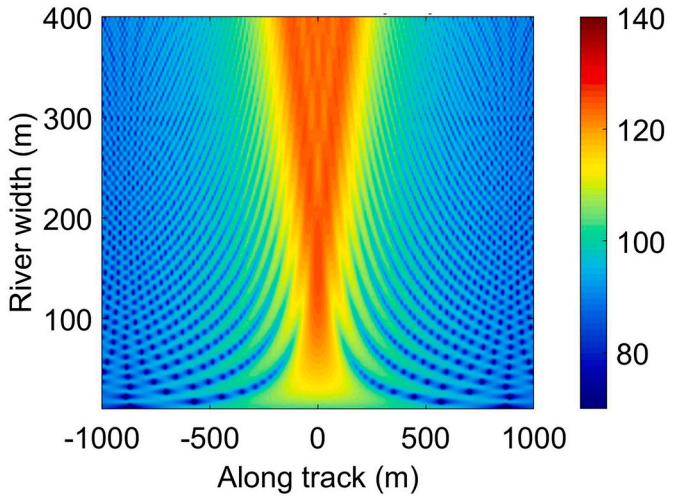

Fig. 3. Along-track specular σ (dBsm) for rectangular 'rivers' of varying widths.

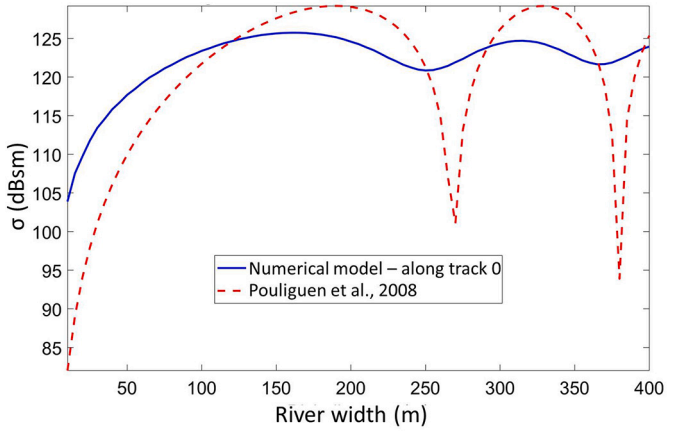

Fig. 4. σ (dBsm) of the numerical model for river midline at nadir. The Pouliguen et al. (2008) model shown is for a disk for comparison with Fig. 2.

with a diameter of *a*. Using the Sentinel-3 parameters ($k = 2\pi/\lambda$ with $R = 815$ km), the maximum σ is 129 dBsm when the disc diameter is one Fresnel zone or $\sqrt{2\lambda R} = 190$ m. Fig. 2 plots the numerically calculated value at CPA and the corresponding Pouliguen et al. RCS. The agreement is <1 dB except in the deep nulls.

In real-world data (discussed in Section 4.1), specular RCS values concentrate at 129 dBsm, which is a remarkable agreement between theory and data. For rectangular rivers, the maximum σ is 125 dBsm (Fig. 4). The maximum is slightly less than the case of the disk shape (lake) because of phase cancellation by elemental scatterers along the length dimension. The maximum σ occurs at a width of 150 m (Fig. 4).

As noted later (Section 4.1), the σ of bare Earth and vegetation is typically <40 dBsm. The RCS of small to large vehicles in the Ku band is in the range of 0 to 30 dBsm (Raynal et al., 2011). Aircraft and large ships are 20–40 dBsm (Skolnik, 1990). Thus, specular echoes are unlikely to be contaminated by nearby clutter or interference.

2.3. Range migration

In all the previous Doppler processing, range migration is applied before coherent sum of a sequence of echoes. Herein, we show that range migration is negligible except for a small constant in the duration when nadir is passing over a water body. The phase of a specular point at the CPA is given as

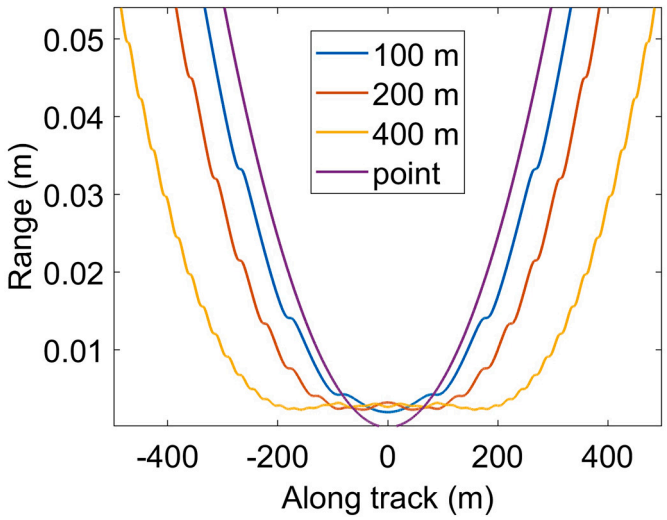

Fig. 5. Exact range migration of a specular river of varying width. The point scatterer curve is the parabolic range migration.

$$\varphi_0 = 2\pi f_c \frac{2R_0}{c} \tag{3}$$

where, as stated in Table 1, f_c is the carrier frequency, R_0 is the range to surface at the nadir and c is the speed of light. The phase of the sum of all elements sensed at an instant in time, relative to the CPA, is given as

$$\varphi_n = argz(n) - \varphi_0 \tag{4}$$

where φ_0 is the phase of a specular echo at the CPA; arg(z(n)) is the phase of the *n'th* echo, so the difference is the phase migration of the *n'th* echo with respect to CPA. The range migration is given as λ *unwrap* $(\varphi_\eta)/4\pi$.

Fig. 5 shows the theoretical range migration for specular rivers of various widths. The parabola is a fair approximation for rivers of <50 m widths. For water bodies of width of ~100 m or greater, the range is approximately constant and slightly biased for the duration of the specular flash. The bias, which is approximately 3 mm, is due to the coherently averaged range over the Fresnel disk, and the range to the edge of the Fresnel disk is 6 mm greater than that at the nadir point; hence, an 'average' of 3 mm is reasonable. Range migration is significant only when the nadir is outside the water boundary; if we confine the PISA to consider only echoes within the flash period when the nadir is over the water body, the range migration can be ignored, and the 3 mm bias can be added as a correction at the end.

3. Precise inland surface altimetry (PISA)

The current workflow for PISA (Fig. 6) is described specifically for the Sentinel-3 altimeters. With slight modifications, the same workflow applies to CryoSat-2 and Sentinel-6, as well as future missions (e.g., CRISTAL).

The Sentinel-3 fires bursts of 64 pulses at a repetition frequency (PRF) of 17.825 kHz over a time interval of 3.6 ms, corresponding to 25.2 m along the track. Bursts are repeated at intervals of 12.7 ms, equivalently to 89 m along track. The IQ data is provided in the Copernicus Open Access Hub, organized in two files for each orbit (for ascending or descending segments). There are approximately 250,000 contiguous bursts in each file. The 64-pulse bursts are stored in I & Q arrays of size 64 × 128 with 8-bit values. We denote the burst $s_n(t)$, $n = 1,2, \ldots,64$ for echo index and $t = 1,2, \ldots,128$ for the fast time index.

Each burst record is accompanied by a set of instrumental calibration variables and satellite ephemerides. The parameters relevant to the PISA are listed in the name-value column in Table 1. It is noted that the burst

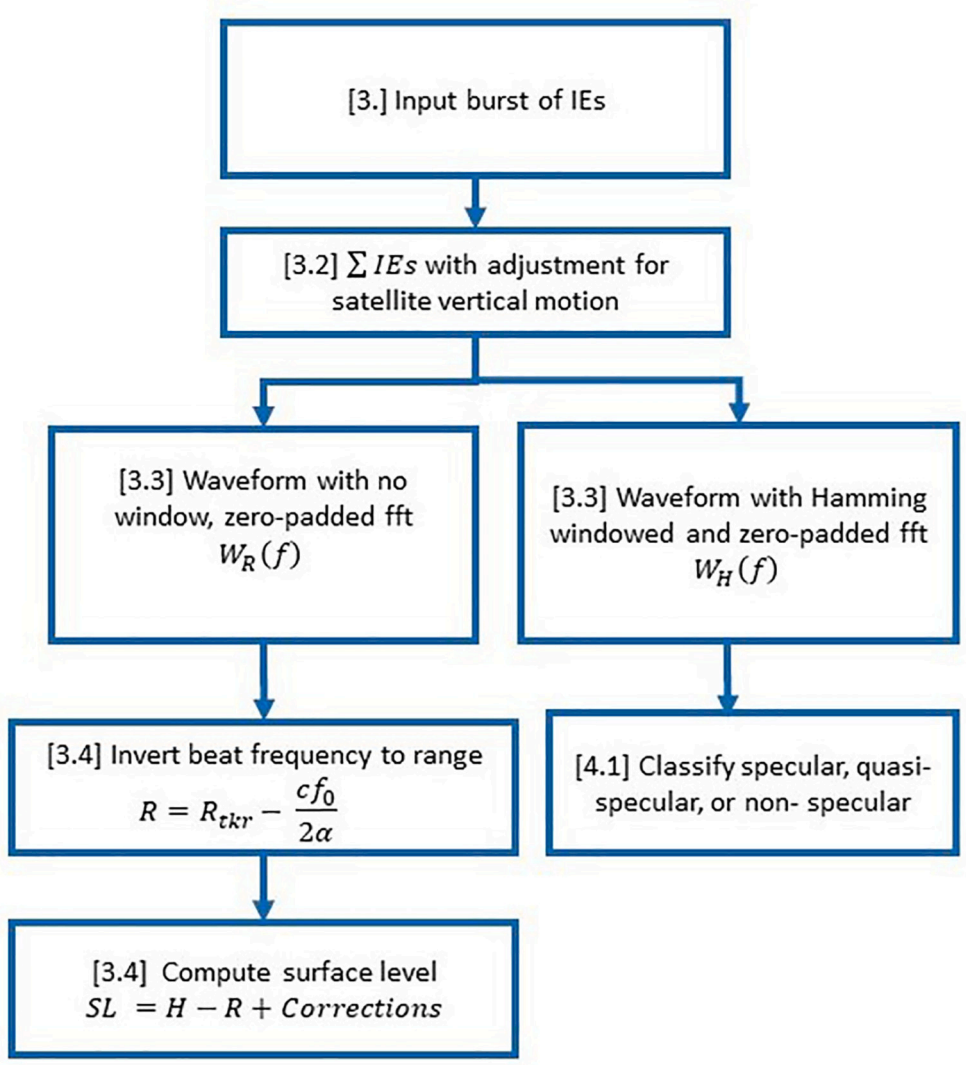

Fig. 6. PISA algorithm flowchart. Reference to sections in the text are in [x.x], e.g. [3.4] refers to Section 3.4 to compute surface level.

ground length, 25 m, is so short that one can consider all 64 echoes within the burst as either on- or off-water. So the entire burst is either processed or not based on the location of the mid echo on the water mask. It is also noted that the minimum specular flash duration, 100 m, is about the same as the interval between bursts. It is thus guaranteed that there will be at least one burst during any river or lake crossing. The foregoing algorithm description and the flow chart processes one burst of IQ data at a time.

The latitude and longitude of each burst are referenced with respect to a water mask derived from high resolution imagery in Google Earth. Bursts over the water are processed as described in the following sub-sections. If there are multiple bursts during a water crossing, the bursts can be either coherently combined or used to measure the surface slope.

3.1. Individual echo (IE)

In the output of the IF stage the n-th IE is mathematically expressed as:

$$s_n(t) = \mathrm{e}^{-i\varphi(t)} \tag{5}$$

$$\varphi(t) = 2\pi\left(f_c\tau' - \left(\alpha\tau' - \frac{2f_c v_r}{c}\right)t + \frac{\alpha}{2}\tau'^2\right) \tag{6}$$

(Egido and Smith, 2016). The parameters used in the above equations are defined in Table 1. Of the four terms in the signal phase, two are related to beat frequency. The beat frequency $f_b = \alpha\tau' - \frac{2f_c v_r}{c}$ is related to the range but has range-Doppler ambiguity. Uncoupling this ambiguity is a well-known issue in FMCW radars for applications with moving targets, such as vehicle collision avoidance. However, in altimetry over flat water, the Doppler is entirely from the satellite vertical motion, which is known and can be regarded as a constant for the duration of a burst. We apply a range correction $f_c v_r/\alpha$ in the final stage of the process flow (Section 3.4).

3.2. Burst integration

The high PRF of the Sentinel-3 was mainly designed for ocean Doppler processing (Le Roy et al., 2007), and this PRF is ~50 times greater than that required for specular targets. The 64 pulses in a burst are almost redundant observations in one Fresnel zone. These pulses can be summed to improve the signal to noise ratio (SNR) by 10 log10(64) = 18 dB. There is a corresponding improvement in the range precision relative to using only one echo.

As noted in Section 2.3, there is no range migration; however, the satellite vertical motion, which can be as much as 8 cm within a burst period, appears in the phase terms, $f_c\tau'$ and $\frac{\alpha}{2}\tau'^2$. The $f_c\tau'$ term is a time delay, relative to the burst midpoint,

$$\Delta\tau_n = \frac{2(n - 32.5)v_r}{cPRF} \tag{7}$$

where 32.5 is the index to the midpoint of a 64-pulse burst. The term $\frac{g}{2}\tau'^2$ is small and can be ignored. The time-delay corrected burst sum is

$$s'(t) = \sum_n s_n(t) e^{-i2\pi f_c \Delta\tau_n} \tag{8}$$

3.3. Waveform

The waveform is computed with and without windowing. The unwindowed waveform expressed in dB is:

$$W_R(f) = 10\, log_{10} |fft(s'(t))|^2 \tag{9}$$

With zero padding of s' to a size of 128 × 469 (=60,032) before applying the fast Fourier transform (FFT), the spectrum is interpolated to a range resolution of 1 mm. The Hamming window W_H is scaled to σ in units of dBsm.

$$W_H = W_H + SigmaScaling + AGC + 5.35 \tag{10}$$

The 5.35 dB adjustment accounts for the Hamming window. The scaling factor (dB) is defined in ESA (2017).

The Hamming window is commonly used in SAR altimetry to minimize corrupting interference from nearby range bins. In PISA there is a different point of view. Assuming interference is negligible the unwindowed waveform is better because it uses the full pulse width. However the windowed waveform is best to assess interference in sidelobes. In a perfect specular return the peak σ is the value predicted by the models (Section 2), and the near sidelobes are −43 dB relative to the peak. Much higher sidelobes indicate that the echo is corrupted and may be unsuitable for range estimation.

3.4. Range and surface level

The beat frequency f_0 can be estimated from s' with a variety of well-known frequency-estimation methods. Herein, we use the peak $W_R(f)$ adjusted by a system constant related to the fact that the R_{tkr} reference range bin is 45; range bin of 45 is equivalent to a beat frequency of −446.428 kHz.

$$f_0 \leftarrow f_0 + 446428\ Hz \tag{11}$$

The range relative to R_{tkr} is

$$\delta R = \frac{f_0 c}{2\alpha} \tag{12}$$

The range solution is

$$R = R_{tkr} - \delta R \tag{13}$$

The range is transformed to a surface level (SL). In altimetry literature, SL is more commonly known as the water level (WL) because most altimetry applications are concerned with ocean and inland waters. The expression for computing SL is

$$SL = (H - R) - \left(\frac{f_c v_r}{\alpha} + \Delta_{cog} + \Delta_{gps} + + \Delta_{geo} + \Delta_{Fz}\right) \tag{14}$$

The $f_c v_r/\alpha$ term is the Doppler-shift effect that needs to be decoupled from the range in altimetry (as explained in Section 3.1), and Δ_{Fz} is the 3 mm range migration bias (Section 2.3). Δ_{cog} is an instrumental correction that accounts for the distance between the antenna and satellite center of mass (CoG). Δ_{gps} is a reference correction for time-independent solid Earth tides (known as permanent tides) that must be applied when surface levels are compared to GPS heights which are given by convention in tide-free system. Δ_{geo} accounts for the ionospheric and tropospheric propagations, and other geophysical corrections. Geophysical corrections are crustal changes (linked to Earth solid and pole tides) when surface levels are compared to water gauges whose measurements are relative to the crust instead of the center of the earth (see Table 1 for more details on these corrections). The sum of all these correction terms varies slowly and can be ignored in a relative change of range over a sequence of bursts, as in the precision analysis that follows.

4. Real-world data

In the following real-world data are used to determine the precision (rmse) for ranging with one 64-echo burst. Multiple bursts may be combined coherently or incoherently for greater precision, or to measure surface slope. As explained in Section 3.3, the range measurements were discretized to 1 mm by our choice of 469× zero-padding. With 1 mm the discretization precision can be no better than $\sqrt{1/12}$ or 0.288 mm assuming uniform error distribution between −1/2 and + 1/2 mm.

The real-world data used here is Sentinel 3A track 167 over South America and adjacent oceans. The overland portion is about 6000 km long and passes over a variety of inland waters. Over Delta Amacuro (Venezuela) and the Amazon region the track encounters rivers of various widths – from less than to many times wider than a Fresnel diameter. There is a fjord on the Chilean coast; large lakes in the high Andes (Lago Uru and Lago Huillinco); and most importantly for evaluating the real-world range precision, the salar de Uyuni. The Sentinel 3 orbit repeats tracks every 27 days. We processed all fifty-two passes between 2016-Apr-20 and 2020-Dec-16, almost four years of revisits.

4.1. Classification of specularity

The Hamming windowed waveform W_H is characterized by two parameters: the peak value scaled to dBsm and peak sidelobe in dB relative to the peak value. Fig. 7 shows the typical waveforms of the specular echoes from the salar de Uyuni in (a) dry and (b) wet months. The black curve is the Fourier transform spectrum of the Hamming window and is the expected waveform of a perfect specular surface; the red curve is a random single burst, and the blue curve is an average of hundreds of

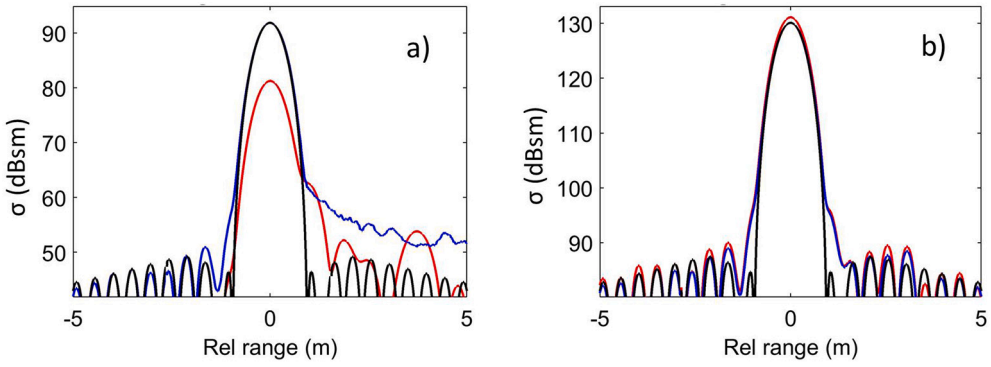

Fig. 7. σ (dBsm) over the dry salar de Uyuni on May 16, 2018 (a) and wet case on February 24, 2018 (b).

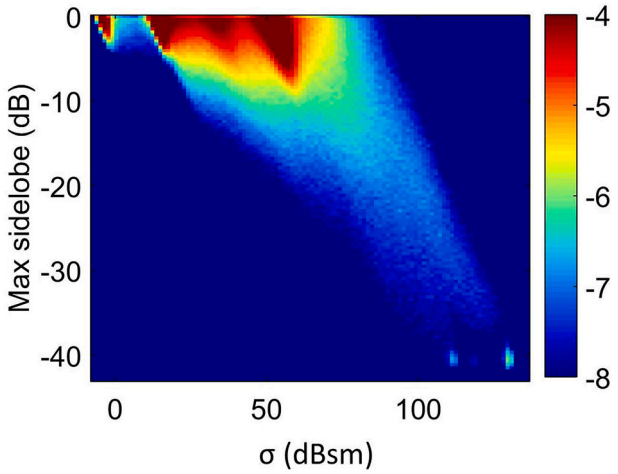

Fig. 8. Joint histogram for specular metrics. The colorbar has units of log probability density.

Table 2
Classification of specular, quasi-specular, and non-specular data for 4,837,038 bursts from 52 passes over South America with the S3A along orbit 167.

Category	σ	Sidelobe	Frequency
Specular	100–130	<−37	0.7%
Quasi-specular	60–120	−37 to −20	5.2%
Non-specular	0–80	> − 20	94%

bursts. In the wet months (Fig. 7b), the typical and average values are almost identical. The peak is at the theoretical maximum of 129 dBsm. In the dry months (Fig. 7a), the waveform is a mixture of specular and rough surface. The specular peak is lower, about 90 dBsm in this case. The elevated levels on the trailing side are as expected for a slightly rough surface (Brown, 1977).

In the wet case, there are slight deviations in the first lobes to the left (leading) and right (trailing) of the peak, where there is a distinct leading–trailing asymmetry. This was observed in all Uyuni specular echoes and also on lakes and rivers. We suspect that the cause is instrumental; however, the exact mechanism is still under investigation. For the time being, we ignore these lobes for the maximum sidelobe parameter. The maximum sidelobe is a level bracketing the peak from −5 to +5 m, excluding the range of −1 to +1 m.

Fig. 8 is the joint histogram (in log probability) of the peak and sidelobe levels for 4,837,038 bursts from 52 passes. The data is mostly overland, but there is some extension into the Caribbean off Venezuela and the South Pacific off Chile. The histogram reveals distinct categories. A simple classification scheme is suggested (with a frequency of occurrence in the South America data) in Table 2. Although a high σ should logically be the main criterion for specularity, it appears that the categories can be better separated by the sidelobe levels.

The specular category can be further divided into weaker (<125 dBsm) and stronger (>125 dBsm) speculars. It is recalled from Section 2.1 that 129 dBsm is the theoretical maximum for specular echoes, and the histogram has a local maximum in the lower-right corner at σ =129 dBsm. This is a remarkable agreement of data and theory. Most echoes (~94%) are either non-specular or thermal noise. The non-specular data has two subcategories, 0–40 dBsm are land echoes and 40–50 dBsm are ocean Brown echoes (Brown, 1977).

Fig. 9 shows the speculars (weaker-yellow, stronger-red) for the 52 passes. The points are compact and overlapping, and one can only obtain a general view of the geographical distribution. The Salar de Uyuni is at a latitude of −20°. Unsurprisingly, there are many speculars in the Amazon basin and Delta Amacuro (Venezuela).

Fig. 10 zooms on four locations of quasi-specular and specular

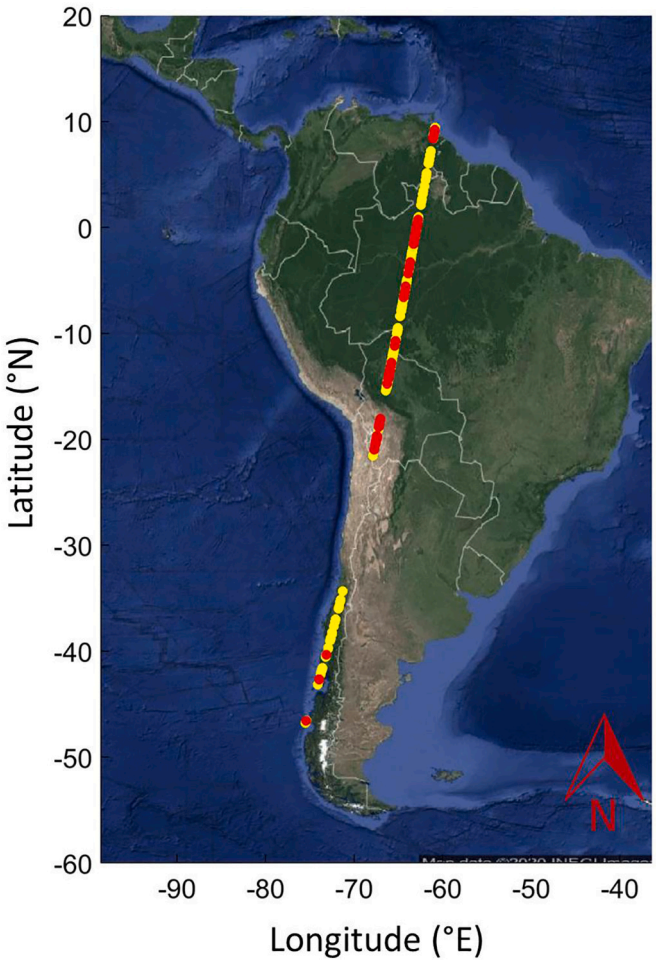

Fig. 9. Locations of specular echoes shown on Google Earth. The yellow dots are weaker speculars (<125 dBsm) and red dots are strong speculars (>125 dBsm).

echoes, which are further discussed in following Sections. Table 3 summarizes the locations studied for range precision.

4.2. *Precision test on the Salar de Uyuni data*

The main approach to measuring the precision is the rmse values of the range estimates in a contiguous series of bursts over a large flat area. We also allow for slow variability due to hydrological and/or geoidal variations. The 9000 sq. km area of the salar de Uyuni is exceptionally well suited for this purpose, and has been used for both radar and LiDAR altimetry evaluations (Verron et al., 2020; Fricker et al., 2005; Sun et al., 2017). It was ground surveyed in two Scripps Institute campaigns in September 2002 (Borsa et al., 2008a) and in September 2009 (Borsa et al., 2019), both in the dry season. Interpolated maps of surface levels from 2002 and 2009 data sets have been provided for this study (A. Borsa, personal communication). The forgoing is our analysis, specifically with the Sentinel 3 and PISA.

The salar de Uyuni has two seasons, wet and dry. Significant precipitation occurs in December–March, peaking in January with an average of 85 mm/month (Sieland, 2014). In this wet period the basin is flooded by rains and inflow from surrounding mountains, to a depth of tens of centimeters; 25 cm reported in Orris (1995), 30–50 cm reported in Bills et al. (2007). Many tourist photos are evidence of a mirror-like water surface (e.g., Unger, 2017) which makes the salar de Uyuni the ideal case to study specular echoes.

The rain season ends abruptly in April; precipitation falls to ~1 mm

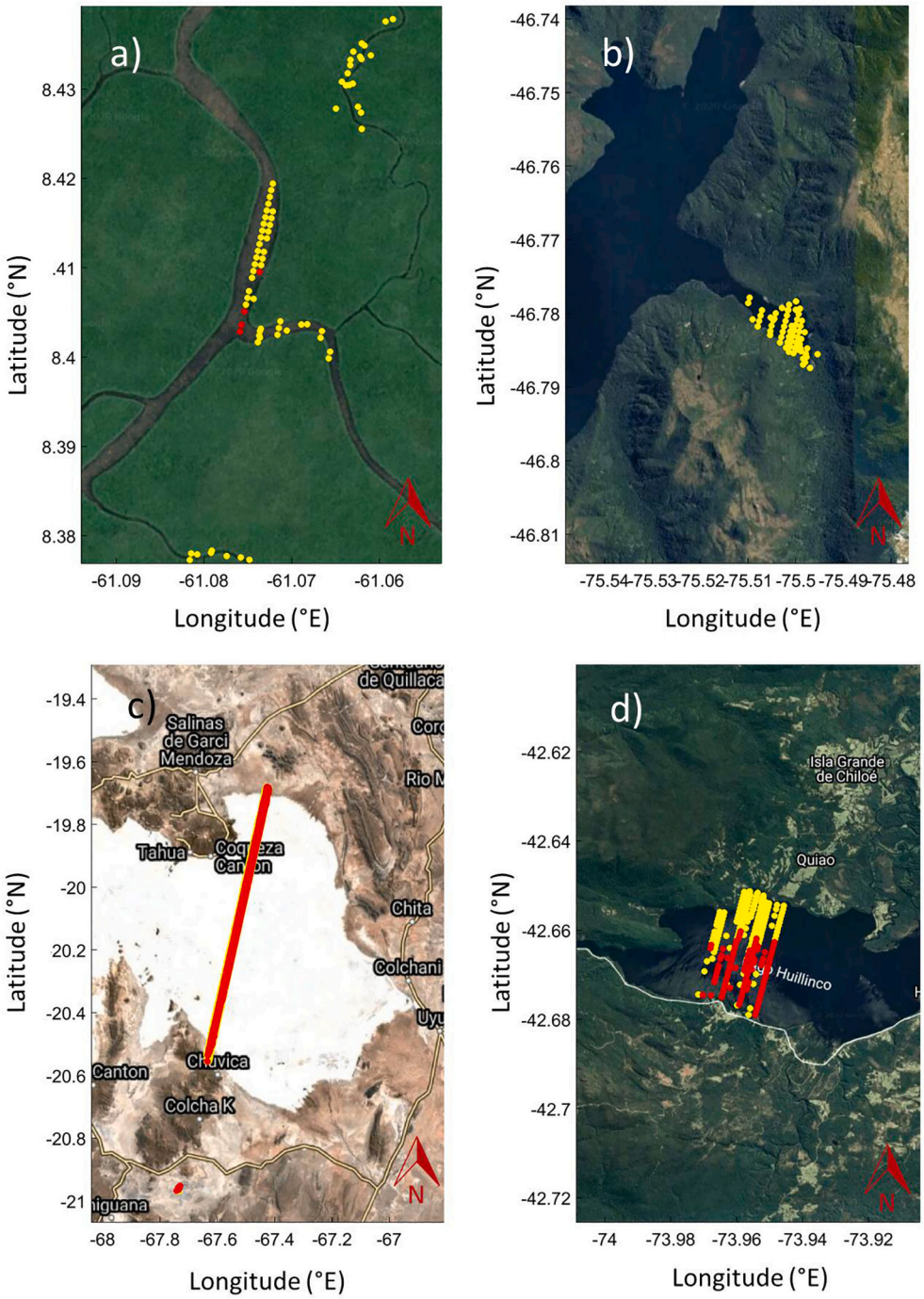

Fig. 10. Google Earth magnified maps for four locations to better illustrate the distributions and frequencies of speculars in these locations. Speculars in a) an unnamed tributary of the Orinoco River, Venezuela; b) a fjord-like channel in south Chile; c) Salar de Uyuni, Bolivia; d) Lago Huillinco, Chile. The red points are stronger speculars (>125 dBsm) and yellow points are weaker speculars (<125 dBsm).

per month; evaporation rate of 2–2.5 mm/d (Borsa et al., 2008a) assures that the basin remains dry and the hard surface is exposed for the duration of the dry seasons, May–November. The surface is crusty, and characterized by desiccation polygons that range between 1 and 4 m (see Fig. 4 in Sieland, 2014).

Six Sentinel 3 tracks cross the salar de Uyuni, two in descending orbits, the others in ascending orbits. Track 167 (descending) was chosen because it crosses the middle with the longest intersection with the Borsa surveys. The foregoing analyses uses the 401 contiguous bursts in a mid-section of the salar de Uyuni basin (latitude −20.4 to −20.1°). Each range measurement was translated to SL (Section 3.4). Precision can then be estimated from the variability in SL. The variability from pass-to-pass can also be used, but with caution, as explained later. An altimetry-to-GPS comparison is also illuminating on the relative precision and spatial resolution. All these analyses are discussed below.

There are several complications in precision analysis. The main complication is the Δgeo correction, which varies from pass to pass with an uncertainty of several centimeter (Fernandes et al., 2014). Another consideration is that the salar de Uyuni is not truly flat; there is a 20 cm North-South level change over the 401 bursts used in the analysis. Furthermore, there is up to 2 km *E*-W drift that may, according to the Borsa GPS model, contributing an additional 0.1 to 1 cm variability in pass-to-pass comparison. In wet months the water level varies temporally and spatially to some unknown degree, but certainly several

Table 3
Summary of locations studied for range precision, showing slope and burst rmse values for the four locations.

Location (Longitude, Latitude)	Sentinel orbit date	Width (Bursts)	dBsm classification	Slope mm/km	Burst rmse (mm)
Salar de Uyuni, Bolivia	S3A 167	12 km	130	5–10	1.3
−67.5 -20.15	2018-02-24	(134)	specular		
	S3A 167	12 km	130		1.5
	2018-03-23	(134)	specular		
	S3A 167	12 km	129–130		1.0
	2019-02-10	(134)	specular		
	S3A 167	12 km	129–130		1.4
	2019-03-09	(134)	specular		
	S3A 167	12 km	70–90		9.5
	2019-09-14	(134)	quasi		
	S3A 167	12 km	70–90		8.0
	2019-10-11	(134)	quasi		
Lago Huillinco, Chile	S3A 167	2 km	110–129	30	1.0
−73.95 -42.67	2016-08-06	(34)	specular		
	S3A 167	2 km	100–130	30	1.6
	2017-09-15	(33)	specular		
	S3A 167	1.8 km	120–129	30	1.2
	2018-02-02	(21)	specular		
Lago Uru Uru, Bolivia	S3A 167	12 km	130	11	0.5
−67.091, −18.114	2017-05-03	(133)	specular		
Tributary of the Orinoco River (Delta Amacuro), Venezuela	S3A 167	2 km	110–120	20	10.1
−61.075 + 8.41	2018-02-24	(23)	specular		

centimeters or more.

In order to eliminate the Δ_{geo} contribution, the SL is set to average zero in the latitude range − 20.18 to −20.16° (64 bursts). This latitude range was determined experimentally to be the flattest portion of the 401-burst stretch. The zero-level adjustment essentially calibrates out all the corrections, but Δ_{geo} in particular since it varies pass-to-pass. The Borsa DEM is zero level adjusted in the same way for altimetry-GPS comparison.

4.2.1. Wet month altimeter passes

The burst level σ values over all 52 passes vary from 70 to 129 dBsm, averaging 95 dBsm. All bursts exhibit a specular or quasi-specular behavior. During wet months σ levels are in the 110 to 129 dBsm range and many echoes are at the theoretical maximum of 129 dBsm. On three dates, 2018-Feb-24, 2019-Feb-10, and 2019-Mar-09, all bursts were within 1 dB of the theoretical maximum. Those are the best dates to assess precision with specular echoes.

Fig. 11a shows the zero-level adjusted SL for 24th February 2018. The other two best dates are similar. The SL values have an N-S trend which includes geoidal and physical surface variations. The ranging rmse is the white noise after the trend is subtracted. We use the variate-difference method with polynomial regression fitting (Quenouille, 1951). The first step subtracts a 5th order polynomial fit which removes most of the trend. The residuals left after detrending, dSL(1), dSL(2), etc., are plotted in 11(b). The quantized steps in dSL are due to the 1 mm quantization in the beat frequency estimates. The second step, computes the variate differences, dSL(1)-dSL(3), dSL(2)-dSL(4), etc., which removes remaining small but perceptible trend. The rmse is then ½ standard deviation of the variate differences; alternatively the rmse is 0.74 MAD of the differences. MAD (median absolute difference) is used if the residuals contain large outliers. In the three wet runs the residuals are Gaussian and the rmse are 0.73, 0.77, and 0.79 mm.

4.2.2. Dry month altimeter passes

In dry months the σ levels are in the 70 to 100 dBsm range, a 30–60 dB reduction from pure specular levels experienced in the wet months. The waveform are quasi-specular by the definition of specularity in Table 2. Fig. 12 shows the zero-level adjusted SL data for the driest

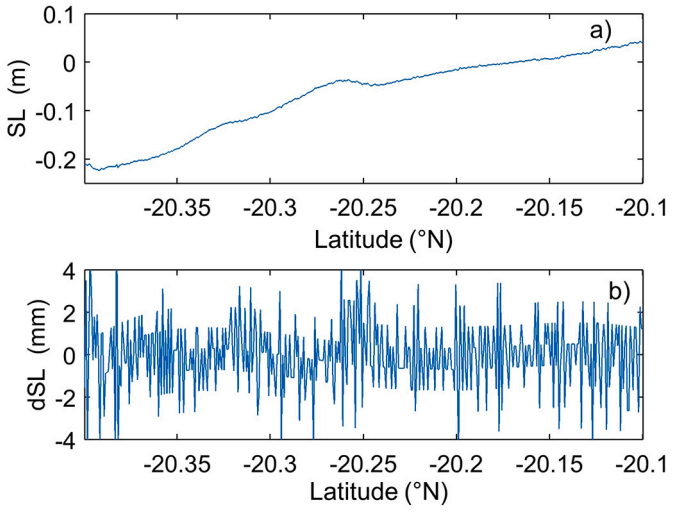

Fig. 11. (a) Zero-level adjusted SL for 24th February 2018 and (b) residuals after detrending.

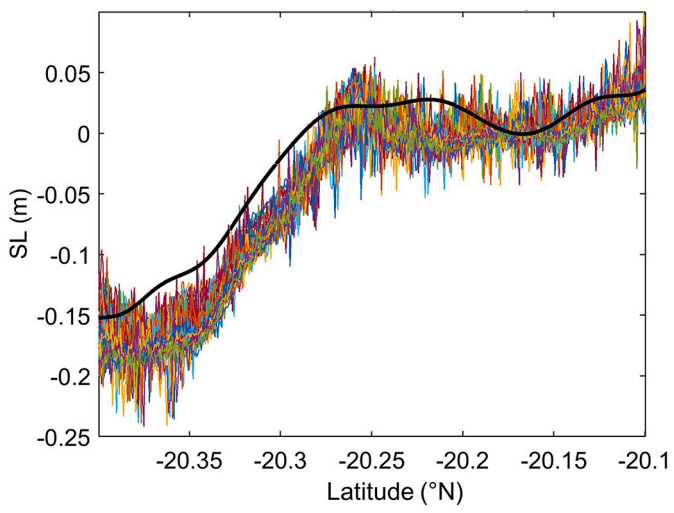

Fig. 12. Zero-level adjusted SL for dry months (April to October). The thick black line is the corresponding Borsa levels, averaged over all dry period tracks.

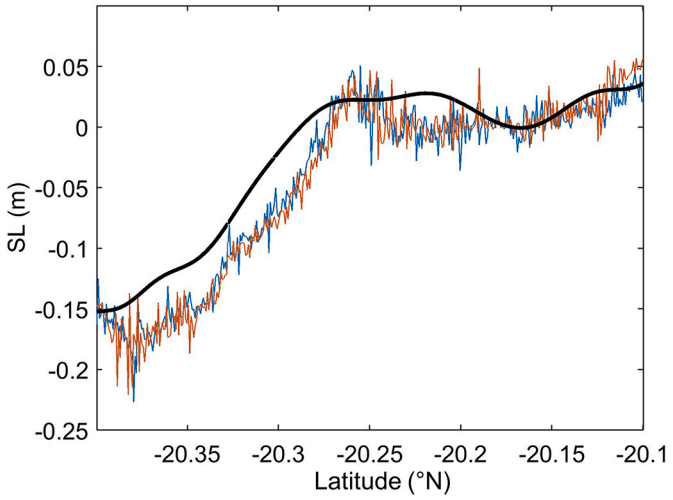

Fig. 13. Zero-level adjusted SL for 2017-August-19 and 2019-August 18. The thick black line is the corresponding Borsa levels, averages over all dry period tracks.

months. For clarity 2% extreme outliers (>5 cm from the trend) are excluded from the plot. A "mound" is now fully exposed and recognizable as a 5-km wide, 5 cm high protrusion at latitude −20.25.

Using the same two-step procedure as in the wet months, the rmse in the dry months is 3–6 mm with MAD, 4–8 mm with standard deviation. It is remarkable that even with the surface roughness of the dry salar de Uyuni the altimetry precision is <1 cm. The thick black line is the corresponding Borsa's DEM averaged over all dry period tracks. Altimeter and Borsa's DEM SLs are in agreement on the 20 cm trend. The radar altimeter appears to better resolve the mound. This is expected since the altimeter spatial resolution is the Fresnel diameter, about 200 m. The DEM model from the Borsa GPS survey has a 6.7 km resolution (Borsa et al., 2008b).

Fig. 12 shows the elevation profile in the 40 dry months passes. Pass-to-pass differences can provide another way to quantify the ranging precision, but the *E*-W track drifts are an additional source of variability (~1 cm).

However, two passes, 2017-August-19 and 2019-August 18 had E-W difference in the altimeter tracks of only 4 m – in other words, virtually identical. The SL profiles for these are shown in Fig. 13. The intra-pass MAD-based rmse are 6.3 mm and 5.6 mm. The MAD rmse from differencing the two passes is 7.4 mm. It is remarkable that the *per burst* rmse from elevation profiles measured two years apart is <1 cm.

4.3. Lago Huillinco

For a similar analysis of the precisions for lakes and rivers, we need specular water bodies with sufficient number of bursts in one pass to obtain meaningful statistics for the rmse. Most rivers are too narrow and provide only one or very few bursts. Larger water bodies have more fetch for wind waves and are less likely to be specular. However, several exceptions were found, and each was analyzed in the same way as the Uyuni data. The range estimates of the contiguous bursts were detrended with a polynomial fit, usually of the 2nd or 3rd order, and the residuals are used to estimate the range rmse values.

Of the 52 passes over the Lago Huillinco (42.67° S, 73.95° E) about 65% are specular or quasi-specular. Fig. 10d shows the specular echoes; there are peculiar and unexplained south to north trends, with weaker echoes more likely on the north side. Three passes were examined in detail (see Table 3). In all these three passes, the range precision was approximately 1 mm, with a 30 mm/km slope from south to north; the σ varies from 100 dBsm on the north shore to 130 dBsm on the south shore.

4.4. Lago Uru Uru

Lago Uru Uru (18.114° S, 67.091° E) is located in the Bolivian Altiplano. This lake is not far from the Salar de Uyuni and is in a similar geography. A pass on 2017-05-03 recorded 133 contiguous specular bursts, with an rmse of 0.5 mm, which is even better than that of the Salar de Uyuni. The water slope was nearly linear at 11 mm/km.

4.5. Orinoco tributary

The Orinoco tributary in Venezuela (Fig. 10a) at 8.413° N, 61.074° E is oriented north–south, and the nadir track extends over the length of the river for 1.6 km. This presented a rare opportunity to evaluate the PISA on a relatively narrow water body with potential land clutter within the Fresnel zone of each echo coming from either the E or W shore. The range rmse was 10.1 mm with a slope of 20 mm/km. The slope agrees with the northerly flow direction.

5. Summary and conclusion

The PISA algorithm proposed here is a special case of the SAR-based altimetry processing methods. The algorithm integrates only echoes when nadir is directly over a river or lake. The salar de Uyuni data provides a benchmark for the best range precision possible with Sentinel-3. For specular echoes the range precision is ~1 mm, and for quasi-specular echoes precision is ~1 cm. In a further validation of the ranging accuracy we found surface elevation profiles two years apart, repeatable to rmse <1 cm. Previously Doppler and LRM reported algorithms have not achieved this level of precision (Benveniste et al., 2019). Hence, the proposed PISA is suggested as the preferred retracking for bursts passing the specularity test.

Specularity is an important consideration for inland altimetry on rivers, lakes, reservoirs, and flood plains. The example of specular echoes from a fjord further suggests usage of PISA in sheltered coastal waters.

Since the specular flash occurs only when the satellite nadir is directly over water, there are large spatial gaps in the ability of satellite altimetry to observe specular water bodies. Considering that the average separation of Sentinel-3 tracks is 25 km, the probability of the nadir crossing a 100 m lake is ~0.4%; for a 1 km wide lake the probability is ~4%. The Surface Water Ocean Topography (SWOT) mission (Biancamaria et al., 2016), hopes to fill such gaps with non-specular water echoes. The proposed French SMall Altimetry Satellites for Hydrology (SMASH) mission decreases the inter-track gaps with a swarm of small satellite altimeters (Verron et al., 2020).

Declaration of Competing Interest

The authors declare that they have no known competing financial interests or personal relationships that could have appeared to influence the work reported in this paper.

Acknowledgments

The authors would like to acknowledge the European Space Agency (ESA) for granting the use of Sentinel-3 data. The authors wish to thank Salvatore Dinardo (CLS, France) for help with understanding the L1A data, Walter Smith (NOAA, US) for discussions since the beginning of the development of the PISA algorithm, and Adrian Borsa (SIO, US) for providing the GPS data over Salar de Uyuni and helping with understanding the data.

References

Abileah, R., Gómez-Enri, J., Scozzari, A., Vignudelli, S., 2013. Coherent ranging with Envisat radar altimeter: a new perspective in analyzing altimeter data using Doppler

processing. Remote Sens. Environ. 139, 271–276. https://doi.org/10.1016/j.rse.2013.08.005.
Abileah, R., Scozzari, A., Vignudelli, S., 2017. Envisat RA-2 individual echoes: a unique dataset for a better understanding of inland water altimetry potentialities. Remote Sens. 9 (6), 605. https://doi.org/10.3390/rs9060605.
Abileah, R., Vignudelli, S., Scozzari, A., 2018. Implications of specular echoes for monitoring of inland water bodies. In: Presentation made at 25 Years Progress in Radar Altimetry, Ponta Delgada, São Miguel Island Azores Archipelago, Portugal, 24–29 September 2018. https://nikal.eventsair.com/QuickEventWebsitePortal/25-years-of-progress-in-radar-altimetry-symposium/esa/ExtraContent/ContentPage?page=8 (Accessed 3 May 2021).
Benveniste, J., Cazenave, A., Vignudelli, S., Fenoglio-Marc, L., Shah, R., Almar, R., Andersen, O., Birol, F., Bonnefond, P., Bouffard, J., Calafat, F., Cardellach, E., Cipollini, P., Dufau, C., Fernandes, J., Garrison, J., Frappart, F., Gommenginger, C., Han, G., Høyer, J.L., Kourafalou, V., Le Cozannet, G., Leuliette, E., Li, Z., Loisel, H., Madsen, K.S., Marcos, M., Melet, A., Meyssignac, B., Pasqual, A., Passaro, M., Ribo, S., Scharroo, R., Song, T., Speich, S., Wilkin, J., Woodworth, P., Wöppelmann, G., 2019. Requirements for a Coastal Hazard Observing System, OceanObs'19 Community White Paper, Frontiers in Marine Science Journal, Specialty Section 'Coastal Ocean Processes', 6, p. 348. https://doi.org/10.3389/fmars.2019.00348.
Berry, P.A.M., Freeman, J.A., Rogers, C., Benveniste, J., 2007. Global analysis of Envisat RA-2 burst mode echo sequences. IEEE Trans. Geosci. Remote Sens. 45 (9), 2869–2874. https://doi.org/10.1109/TGRS.2007.902280.
Biancamaria, S., Lettenmaier, D.P., Pavelsky, T.M., 2016. The SWOT mission and its capabilities for land hydrology. Surv. Geophys. 37 (2), 307–337. https://doi.org/10.1007/s10712-015-9346-y.
Bills, B., Borsa, A., Comstock, R.L., 2007. MISR-based passive optical bathymetry from orbit with few-cm level of accuracy on the Salar de Uyuni, Bolivia. Remote Sens. Environ. 107, 240–255. https://doi.org/10.1016/j.rse.2006.11.006.
Borsa, A.A., Bills, B.G., Minster, J.B., 2008a. Modeling the topography of the Salar de Uyuni, Bolivia, as an equipotential surface of Earth's gravity field. J. Geophys. Res. Solid Earth 113, B10408. https://doi.org/10.1029/2007JB005445.
Borsa, A.A., Fricker, H.A., Bills, B.G., Minster, J.B., Carabajal, C.C., Quinn, K.J., 2008b. Topography of the Salar de Uyuni, Bolivia from kinematic GPS. Geophys. J. Int. 172 (1), 31–40. https://doi.org/10.1111/j.1365-246X.2007.03604.x.
Borsa, A.A., Fricker, H.A., Brunt, K.M., 2019. A terrestrial validation of ICESat elevation measurements and implications for global reanalyses. IEEE Trans. Geosci. Remote Sens. 57 (9), 6946–6959. https://doi.org/10.1109/TGRS.2019.2909739.
Brown, G., 1977. The average impulse response of a rough surface and its applications. IEEE Trans. Antennas Propag. 25 (1), 67–74. https://doi.org/10.1109/TAP.1977.1141536.
Collins, M.J., Raney, R.K., Livingstone, C.E., 1998. On the model–based estimation of backscatter texture from SAR image texture for area–extensive scenes. Proc. R. Soc. Lond. Ser. A: Math. Phys. Eng. Sci. 454 (1979), 2859–2891.
Dinardo, S., 2020. Techniques and Applications for Satellite SAR Altimetry over Water, Land and Ice (Doctoral dissertation, Technische Universität). Technische Universität Darmstadt, p. 185. https://doi.org/10.25534/tuprints-00011343.
Egido, A., Smith, W.H., 2016. Fully focused SAR altimetry: theory and applications. IEEE Trans. Geosci. Remote Sens. 55 (1), 392–406. https://doi.org/10.1109/TGRS.2016.2607122.
ESA, 2017. Sentinel-3 Core PDGS Instrument Processing Facility (IPF) Implementation Product Data Format Specification - SRAL/MWR Level 1 & 2 Instrument Products, Ref: S3IPF.PDS.003 Issue: 2.9, p. 249. Available at. https://earth.esa.int/documents/247904/1848151/Sentinel-3_Product_Format_Specification_SRAL-MWR_L1-2.
Fernandes, M.J., Lázaro, C., Nunes, A.L., Scharroo, R., 2014. Atmospheric corrections for altimetry studies over inland water. Remote Sens. 6 (6), 4952–4997. https://doi.org/10.3390/rs6064952.
Fricker, H.A., Borsa, A., Minster, B., Carabajal, C., Quinn, K., Bills, B., 2005. Assessment of ICESat performance at the Salar de Uyuni, Bolivia. Geophys. Res. Lett. 32 (21) https://doi.org/10.1029/2005GL023423.
Fu, L.L., Cazenave, A., 2000. Satellite Altimetry and Earth Sciences: A Handbook of Techniques and Applications (Vol. 69). Elsevier.
Kleinherenbrink, M., Naeije, M., Slobbe, C., Egido, A., Smith, W., 2020. The performance of CryoSat-2 fully-focussed SAR for inland water-level estimation. Remote Sens. Environ. 237, 111589. https://doi.org/10.1016/j.rse.2019.111589.
Le Roy, Y., Deschaux-Beaume, M., Mavrocordatos, C., Aguirre, M., Heliere, F., 2007. SRAL SAR radar altimeter for sentinel-3 mission. In: Proceedings of IEEE International Geoscience and Remote Sensing Symposium, Barcelona, Spain, 23–27 July 2007, pp. 219–222. https://doi.org/10.1109/IGARSS.2007.4422769.
Murphy, A.B., 2006. Modified Kubelka–Munk model for calculation of the reflectance of coatings with optically-rough surfaces. J. Phys. D. Appl. Phys. 39 (16), 3571. https://doi.org/10.1088/0022-3727/39/16/008.
Orris, G.J., 1995. Bibliography and Summary of Data available for the Salar de Uyuni, Bolivia Open File Report. U.S. Geological Survey, 95-18. https://doi.org/10.3133/ofr95618 (16 pp).
Pekel, J.F., Cottam, A., Gorelick, N., Belward, A.S., 2016. High-resolution mapping of global surface water and its long-term changes. Nature 540 (7633), 418–422. https://doi.org/10.1038/nature20584.
Pouliguen, P., Hémon, R., Bourlier, C., Damiens, J.F., Saillard, J., 2008. Analytical formulae for radar cross section of flat plates in near field and normal incidence. Prog. Electromagn. Res. 9, 263–279. https://doi.org/10.2528/PIERB08081902.
Quartly, G.D., Passaro, M., 2015. Initial examination of AltiKa's individual echoes. Mar. Geod. 38 (Suppl. 1), 73–85. https://doi.org/10.1080/01490419.2014.984882.
Quenouille, M.H., 1951. The variate-difference method in theory and practice. Rev. Int. Stat. Inst. 19 (2) https://doi.org/10.2307/1401239.
Raney, R.K., 1988. The delay/Doppler radar altimeter. IEEE Trans. Geosci. Remote Sens. 36 (5), 1578–1588. https://doi.org/10.1109/36.718861.
Raynal, A.M., Bickel, D.L., Denton, M.M., Bow, W.J., Doerry, A.W., 2011. Radar cross section statistics of ground vehicles at Ku-band. In: Proceedings of International Society for Optics and Photonics (SPIE)Radar Sensor Technology Conference XV, 25-29 April 2011, Orlando, US, 8021E. https://doi.org/10.1117/12.882875.
Sieland, R., 2014. Hydraulic Investigations of the Salar de Uyuni, Bolivia. Thesis of Technische Universität Bergakademie Freiberg, p. 208. http://tu-freiberg.de/sites/default/files/media/institut-fuer-geologie-718/pdf/fog_volume_37.pdf (Accessed 31 March 2021).
Skolnik, M.I., 1990. Introduction to Radar Systems. McGraw-hill, New-York, p. 640.
Sun, X., Abshire, J.B., Borsa, A.A., Fricker, H.A., Yi, D., DiMarzio, J.P., Paolo, F.S., Brunt, K.M., Harding, D.J., Neumann, G.A., 2017. ICESAT/GLAS altimetry measurements: received signal dynamic range and saturation correction. IEEE Trans. Geosci. Remote Sens. 55 (10), 5440–5454. https://doi.org/10.1109/TGRS.2017.2702126.
Unger, E., 2017. These Salt Flats Are One of the Most Remarkable Vistas on Earth. National Geographic. May 3, 2017. https://www.nationalgeographic.com/travel/article/how-to-see-salar-de-uyuni-salt-flats-bolivia#:~:text=Bolivia%27s%20Salar%20de%20Uyuni,prehistoric%20lakes%20evaporated%20long%20ago (Accessed 30 March 2021).
Verron, J., Bonnefond, P., Andersen, O., Ardhuin, F., Bergé-Nguyen, M., Bhowmick, S., Blumstein, D., Boy, F., Brodeauh, L., Crétaux, J.F., Dabate, M.L., Dibarbour, G., Fleury, S., Garnier, F., Gourdeau, L., Marks, K., Queruel, N., Sandwell, D., Smith, W. H.F., Zaron, E.D., 2020. SARAL/AltiKa mission: a step forward to the future of altimetry. Adv. Space Res. https://doi.org/10.1016/j.asr.2020.01.030. In Press.